Corrosion Science 69 (2013) 311–321

Contents lists available at SciVerse ScienceDirect

Corrosion Science

journal homepage: www.elsevier.com/locate/corsci

# Correlation between the corrosion resistance and the semiconducting properties of the oxide film formed on AZ91D alloy after solution treatment

Mara Cristina Lopes de Oliveira [a], Viviam Serra Marques Pereira [b], Olandir Vercino Correa [c], Nelson Batista de Lima [c], Renato Altobelli Antunes [b,*]

[a] Electrocell Ind. Com. Equip. Elet. LTDA, Technology, Entrepreneurship and Innovation Center (CIETEC), 05508-000 São Paulo, SP, Brazil
[b] Engineering, Modeling and Applied Social Sciences Center (CECS), Federal University of ABC (UFABC), 09210-170 Santo André, SP, Brazil
[c] IPEN/CNEN-SP, Av. Prof. Lineu Prestes 2242, CEP 05508-900 São Paulo, SP, Brazil

ARTICLE INFO

*Article history:*
Received 19 July 2012
Accepted 3 December 2012
Available online 29 December 2012

*Keywords:*
A. Magnesium
B. EIS
B. Polarization

ABSTRACT

The corrosion resistance and semiconducting properties of the oxide film formed on the AZ91D alloy were evaluated. The alloy was tested in the as-cast condition and after a solution annealing treatment. Electrochemical impedance spectroscopy measurements and potentiodynamic polarization curves were obtained in a $H_3BO_3$ (0.05 M) + $Na_2B_4O_7{\cdot}10H_2O$ (0.075 M) solution with pH = 9.2 at room temperature. The semiconducting properties of the oxide film were evaluated using Mott–Schottky plots. The corrosion resistance of the AZ91D was reduced after the solution treatment while the semiconducting properties of the passive films were little affected.



## 1. Introduction

As magnesium has the lowest density among the metals used as structural materials, its specific strength and stiffness overwhelm the performance of conventional light alloys [1]. Consequently, magnesium alloys are very attractive materials for engineering applications where weight reduction is of prime importance such as in the aerospace and automotive industries [2]. In addition, the attributes of magnesium alloys also include high damping capacity, thermal and electrical conductivity, good machinability and electromagnetic shielding thus expanding their market possibilities to areas such as information technology industries and housings for electronics [3,4]. Recently, the intrinsic biocompatibility of magnesium has been explored to the development of biomedical devices, especially regarding temporary fixation implants [5,6]. In spite of these superlative properties, it is well-known that magnesium alloys are highly reactive and easily corrode in a variety of practical environments [7,8]. This critical drawback is a serious obstacle to the expansion of their engineering applications [9].

The AZ91 series, which is alloyed with Al and Zn, is comprised of typical materials for automotive applications [10]. AZ91D is the most widespread material of this series. It is comprised of the α-Mg matrix and a eutectic phase which consists of alternate lamellae of α-Mg and the intermetallic β phase ($Mg_{17}Al_{12}$) [11]. The α-Mg has an anodic character while the β phase is cathodic. Thus, there is a tendency for the corrosion of the α-Mg due to the formation of microgalvanic cells [12]. The distribution of the β phase was found to determine the corrosion resistance of Mg–Al alloys [13]. Therefore, the corrosion rate of the AZ91D alloy can be effectively controlled by properly designing heat treatments. The partial or complete removal of the β phase during a solution treatment may lead to marked alterations of the overall corrosion behavior of the alloy. Zhou et al. [14] have demonstrated that the corrosion resistance of the AZ91D decreased after a solution treatment due to the dissolution of the β phase. Song et al. [15] evidenced the major role of the β phase on the corrosion resistance of the AZ91D alloy. The volume fraction and the continuous distribution of the β phase within the α-Mg matrix were beneficial to the corrosion behavior of the alloy.

In spite of the several investigations regarding the corrosion mechanisms of AZ91D and their relation with the microstructure of the alloy [16–18], few reports are devoted to the study of the correlation between the corrosion resistance and the semiconducting properties of the oxide films formed on this material [19,20]. In this context, the understanding of the effect of solution treatments on the electronic properties of the oxide films formed on the AZ91D alloy is not found in the current literature. The aim of this work was to study the correlation between the corrosion resistance and the semiconducting properties of the oxide film formed on the AZ91D after a solution treatment.

* Corresponding author. Tel./fax: +55 11 4996 8241.
*E-mail address:* renato.antunes@ufabc.edu.br (R.A. Antunes).

0010-938X/$ - see front matter © 2012 Elsevier Ltd. All rights reserved.
http://dx.doi.org/10.1016/j.corsci.2012.12.015

## 2. Experimental

### 2.1. Material and heat treatment

The specimens were cut from a die-cast ingot of the AZ91D alloy kindly provided by Rima Industrial Magnésio S/A, Brazil. The nominal chemical composition of the alloy (by wt.%) was 8.3–9.7% Al, 0.35–1.0% Zn, 0.15–0.30% Mn, <0.10% Si, <0.005% Fe, <0.030% Cu, <0.002% Ni and Mg as the remainder. After cutting, the specimens were solution annealed (T4) under argon atmosphere at 445 °C during 24 h followed by water quenching.

### 2.2. Microstructural characterization

The effect of the heat treatment on the microstructure of the alloy was evaluated through optical microscopy (Olympus microscope) and scanning electron microscopy (SEM LEO 440i). Both as-cast and solution annealed specimens were observed. Cross-sectional views were obtained using a Hitachi TM3000 microscope.

### 2.3. X-ray diffractometry

X-ray diffraction (XRD) measurements were used to characterize the phases of the AZ91D alloy in the as-cast and solution annealed conditions using a Rigaku diffractometer with Cu Kα radiation.

### 2.4. Electrochemical tests

The working electrodes for the electrochemical tests were prepared by encapsulating the specimens into cold cure epoxy resin. The specimens were prepared by mechanical grinding with progressively finer SiC paper up to 1000 grit size. All the electrochemical measurements were performed with an Autolab PGSTAT 100 potentiostat/galvanostat. The electrolyte employed for the measurements was a buffer solution of composition $H_3BO_3$ (0.05 M) + $Na_2B_4O_7{\cdot}10H_2O$ (0.075 M) and pH = 9.2 at room temperature. This electrolyte is traditionally employed for investigating the semiconducting properties of oxide films on different metallic alloys due to stable condition of the film in the buffer solution [19,21]. Thus, we adopted this electrolyte for all the electrochemical tests conducted in this work aiming at investigating the correlation between the corrosion resistance and the semiconducting properties of the oxide film formed on the surface of the AZ91D alloy in a stable solution. A conventional three-electrode cell was used for all the electrochemical tests with a platinum wire as the counter-electrode, a standard calomel electrode (SCE) as the reference and the AZ91D alloy as the working electrode. All the potentials mentioned in the text are referred to the SCE. As-cast specimens were also tested for comparison. All the electrochemical tests were conducted in triplicate to examine the reproducibility of the results. The data presented throughout this text are representative of the electrochemical behavior observed for each condition.

#### 2.4.1. Electrochemical impedance spectroscopy (EIS)

Before every experiment the open circuit potential was monitored for 1 h to ensure a stable electrochemical condition. EIS measurements were performed over the frequency range of 100 kHz to 10 mHz, with an acquisition of 10 points per decade of frequency, at the open circuit potential (OCP), and an amplitude of the perturbation signal of 10 mV (rms). The measurements were carried out after 1, 7, 14 and 21 days of immersion in the electrolyte. The results are given as Nyquist plots.

#### 2.4.2. Potentiodynamic polarization curves

Potentiodynamic polarization curves were obtained for specimens immersed during 1, 7, 14 and 21 days of immersion in the electrolyte, using a scanning rate of $1\ mV\ s^{-1}$. The potential range was from −0.5 V up to +0.5 V versus the open circuit potential. The curves were obtained right after the EIS measurements. A set of three different specimens was polarized at each period of immersion. The results present here are representative of the mean electrochemical behavior observed for each period.

#### 2.4.3. Semiconducting properties of the oxide film (Mott–Schottky analysis)

According to the Mott–Schottky theory the semiconducting properties of oxide films can be studied by measuring the capacitance of the interface layer developed in the oxide film and the Helmholtz layer, as a function of the applied electrode potential when the electrode is immersed in an electrolyte. The measured capacitance ($C$) of the film–electrolyte interface can be described by Eq. (1), where $C_{sc}$ is the space charge capacitance and $C_H$ is the classical Helmholtz capacitance.

$$\frac{1}{C^2} = \frac{1}{C_{SC}} + \frac{1}{C_H} \tag{1}$$

The capacitance of the space charge layer is very small compared to that of the Hemlholtz layer. Then, the measured capacitance can be assumed to be that of the space charge layer when the potentials are applied at a sufficiently high frequency. Hence, the interface oxide film/electrolyte may be described by the Mott–Schottky relation that is shown in Eq. (2) which is valid for a p-type semiconductor:

$$\frac{1}{C^2} = \frac{2}{\varepsilon\varepsilon_0 e N_q}\left(-U + U_{fb} + \frac{kT}{e}\right) \tag{2}$$

In this expression $C$ is the capacitance of the oxide film/electrolyte interface, $U$ is the applied potential, $\varepsilon$ is the dielectric constant of the oxide film, $\varepsilon_0$ is vacuum permittivity, $N_q$ is the doping density (for donors or acceptors, depending if it is related to an n-type or p-type semiconductor, respectively), $e$ is the elementary charge, $k$ the Boltzmann constant, $T$ the absolute temperature and $U_{fb}$ the flat band potential. The plot of $C^{-2}$ versus the applied potential $U$ is called Mott–Schottky plot. The slope of this plot is associated with the semiconducting behavior of the oxide film. Positive slope is typical of n-type semiconductors while negative slope is typical of p-type semiconductors. Doping densities in the oxide film are calculated from the slope of Mott–Schottky plots if its dielectric constant ε is known. In this work the Mott–Schottky approach was used to determine the electronic properties of the oxide film formed on the surface of the AZ91D electrodes. The plots were obtained after 1, 7, 14 and 21 days of immersion in the electrolyte. A set of three different specimens was tested at each period of immersion. The results presented here are representative of the mean electrochemical behavior observed for each period. Capacitance measurements were performed at a fixed frequency of 1 kHz. The working electrodes were polarized in the cathodic direction in successive steps of $50\ mV_{SCE}$ from $2000\ mV_{SCE}$ up to − $1000\ mV_{SCE}$. Doping densities in the oxide film were determined from the slope of straight lines in the Mott–Schottky plots, using the following parameters: $e = 1602 \times 10^{-19}$ C; $\varepsilon_0 = 885 \times 10^{-14}\ F\ cm^2$ [22]; $\varepsilon = 9.6$ for MgO [23].

## 3. Results and discussion

### 3.1. Microstructural analysis

Optical micrographs of the as-cast and solution annealed AZ91D alloy are shown in Fig. 1a and b, respectively. The microstructure of

the as-received ingot presents a dual phase character, consisting of the α-Mg matrix and the eutectic phase distributed along the grain boundaries of the matrix. After solution annealing at 445 °C for 24 h the eutectic phase is dissolved. The eutectic phase is more clearly seen in the SEM micrograph shown in Fig. 1c. This phase consists of large β-$Mg_{17}Al_{12}$ phase particles and the eutectic α-Mg phase. Other authors have confirmed these typical microstructural characteristics of the AZ91D alloy [14,15]. The α-Mg matrix is identified as region 2 in Fig. 1c, whereas a representative β phase portion is marked as region 1. The approximate compositions of each phase were confirmed through energy dispersive X-ray (EDX) analysis, as observed in Fig. 1e (α-Mg) and 1f (β phase). Some residual β phase remained after the solution treatment as clearly seen in Fig. 1d.

### 3.2. X-ray diffractometry (XRD)

X-ray diffraction patterns of the as-cast and SA AZ91D alloy are shown in Fig. 2. The as-cast specimen showed the presence of the α-Mg phase and the β-$Mg_{17}Al_{12}$ phase. After solution annealing, the β phase was dissolved and only the peaks of the α-Mg could be identified in the diffraction pattern of the SA specimen. The residual β phase observed after solution annealing (Fig. 1b) was not detected by XRD measurements due to significant reduction of its volume fraction after the heat treatment.

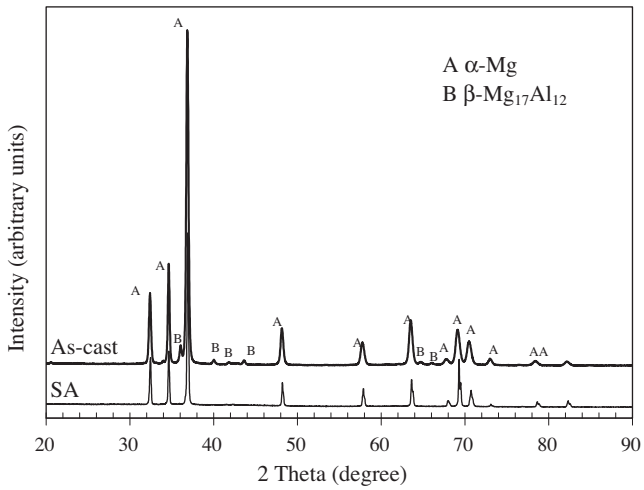


**Fig. 2.** X-ray diffraction patterns of the as-cast and SA AZ91D alloy.

### 3.3. Electrochemical tests

#### 3.3.1. EIS measurements

Before the experiments the open circuit potential was monitored for 1 h to ensure electrochemical stability. Representative

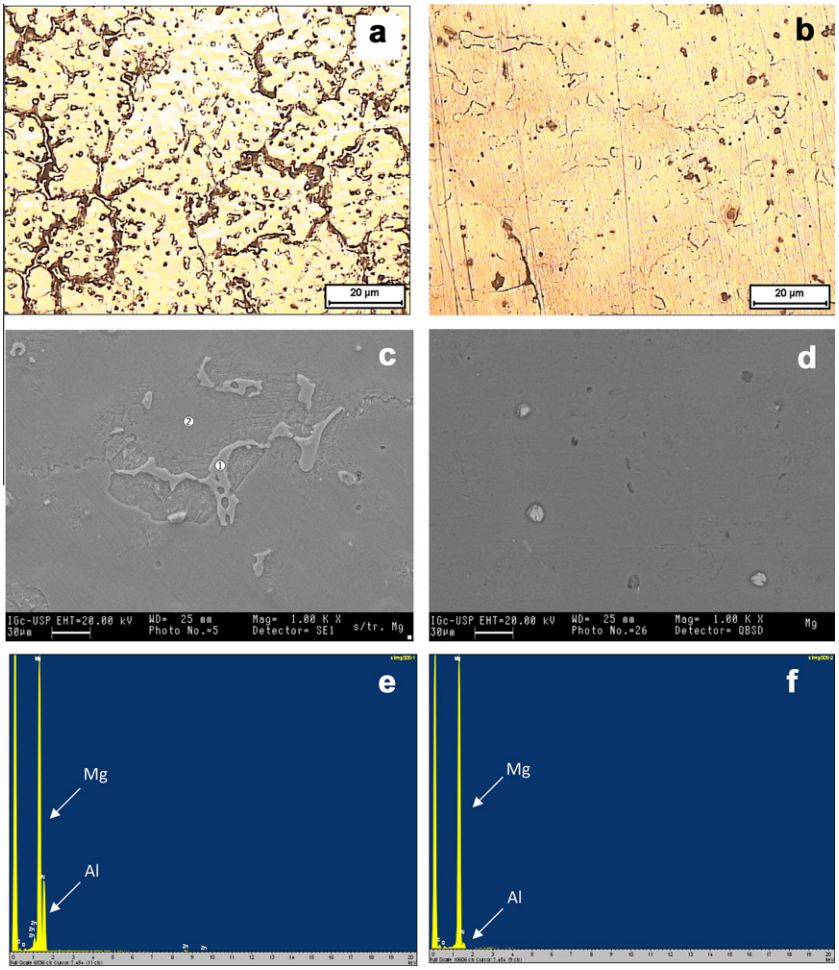


**Fig. 1.** Microstructure of the AZ91D: (a) optical micrograph an as-cast specimen; (b) optical micrograph of a specimen that was solution annealed at 445 °C for 24 h; (c) SEM micrograph an as-cast specimen; (d) SEM micrograph of a specimen after solution annealing; (e) EDX spectrum of region 2 in Fig. 1c; and (f) EDX spectrum of region 1 in Fig. 1c.

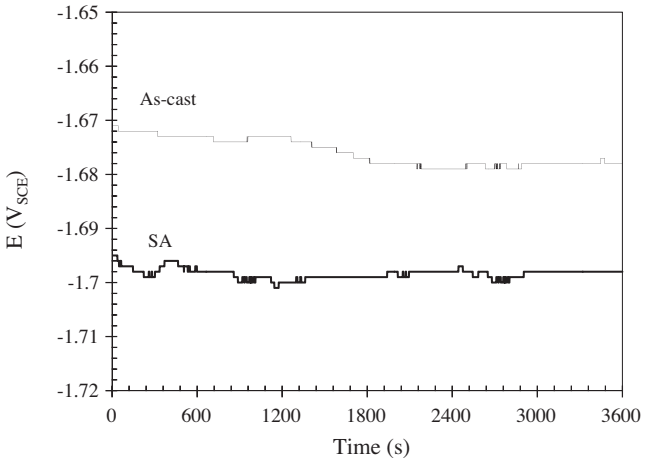


**Fig. 3.** Example of the variation of the open circuit potential versus time for as-cast and solution specimens immersed for 1 day in 0.05 M $H_3BO_3$ + 0.075 M $Na_2B_4O_7 \cdot 10H_2O$ solution with pH = 9.2 at room temperature. Potential monitored during 1 h before the EIS measurements.

results of this procedure are shown in Fig. 3 for as-cast and solution annealed specimens for 1 day of immersion in the testing electrolyte. The variation of the open circuit potential was found to be negligible for during the monitoring, ensuring a stable condition for the EIS measurements. A similar variation was observed for the specimens immersed for longer periods. Nyquist plots of the as-cast and solution annealed (SA) specimens obtained after 1, 7, 14 and 21 days of immersion in 0.05 M $H_3BO_3$ + 0.075 M $Na_2B_4O_7 \cdot 10H_2O$ solution with pH = 9.2 at room temperature are shown in Fig. 4.

The EIS response for 1 day of immersion (Fig. 4a) resembles that of pure Mg [24,25]. Galicia et al. [26] have observed that the impedance diagrams of AZ91 alloy were similar to those of pure Mg. The same behavior was reported by Baril et al. [27]. The diagrams for the as-cast and SA specimens are characterized by two well-defined capacitive loops in the high frequency (HF) and medium frequency (MF) regions. An ill-defined inductive loop seems to be present in the low frequency (LF) part of the diagrams. Inductive loops are frequently reported for Nyquist plots of Mg alloys [28,29]. The inductive behavior is associated with the presence of adsorbed species on the surface of the electrode such as $Mg(OH)_{2ads}$ [30] or $Mg^{2+}_{ads}$ [24]. According to Anik and Celikten [31], the LF inductive loop tends to disappear when the dissolution rate of the alloy decreases due to the formation of a protective oxide film. The low impedance values for the as-cast and SA specimens of the AZ91D observed in the Nyquist plots obtained after 1 day of immersion indicate that the oxide film formed on the surface of the specimens is not protective. The shape of the Nyquist plots are similar to those obtained by Galicia et al. [26] for the AZ91 alloy in a 1 mM $Na_2SO_4$ solution after 36 h of immersion. In this regard, the HF capacitive loop can be ascribed to the charge transfer resistance. The MF time constant is due to diffusion processes through the corrosion oxide layer. Finally, the inductive loop relates to the relaxation of absorbed species. The corrosion resistance of an electrode is associated with the combined diameters of the capacitive loops [32]. Hence, it is seen that the heat treatment did not significantly alter the corrosion resistance of the AZ91D alloy after 1 day of immersion.

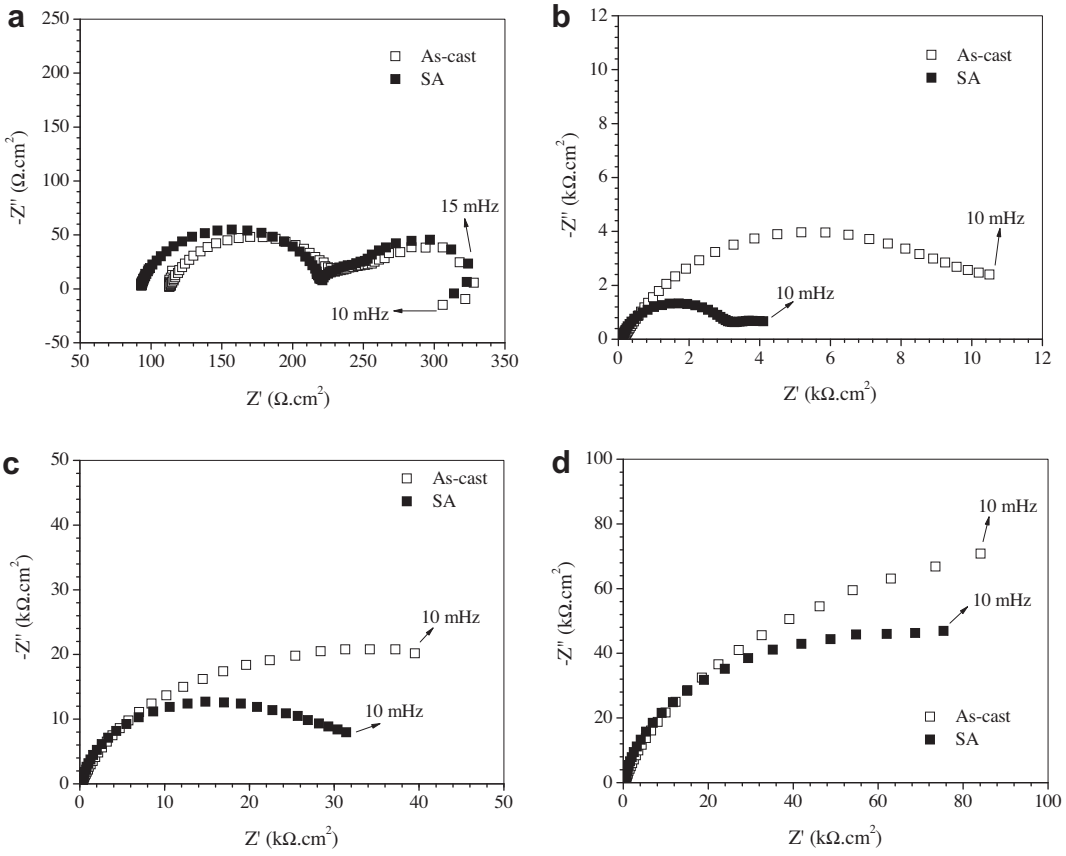


**Fig. 4.** Nyquist plots of the as-cast and solution annealed specimens in 0.05 M $H_3BO_3$ + 0.075 M $Na_2B_4O_7 \cdot 10H_2O$ solution with pH = 9.2 at room temperature after different periods of immersion: (a) 1 day; (b) 7 days; (c) 14 days; and (d) 21 days.

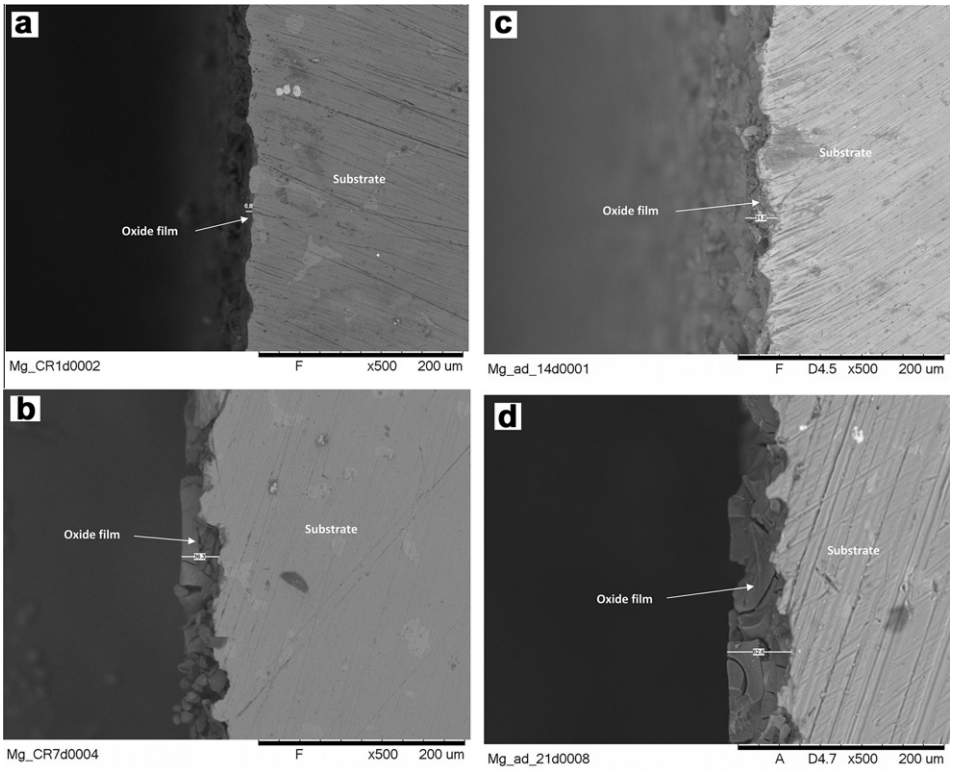


**Fig. 5.** SEM micrographs of the cross-sections of the as-cast specimens after different periods of immersion in 0.05 M $H_3BO_3$ + 0.075 M $Na_2B_4O_7{\cdot}10H_2O$ solution with pH = 9.2 at room temperature: (a) 1 day; (b) 7 days; (c) 14 days; and (d) 21 days. The thicknesses of the oxide films are indicated in the micrographs (the values are in micrometers).

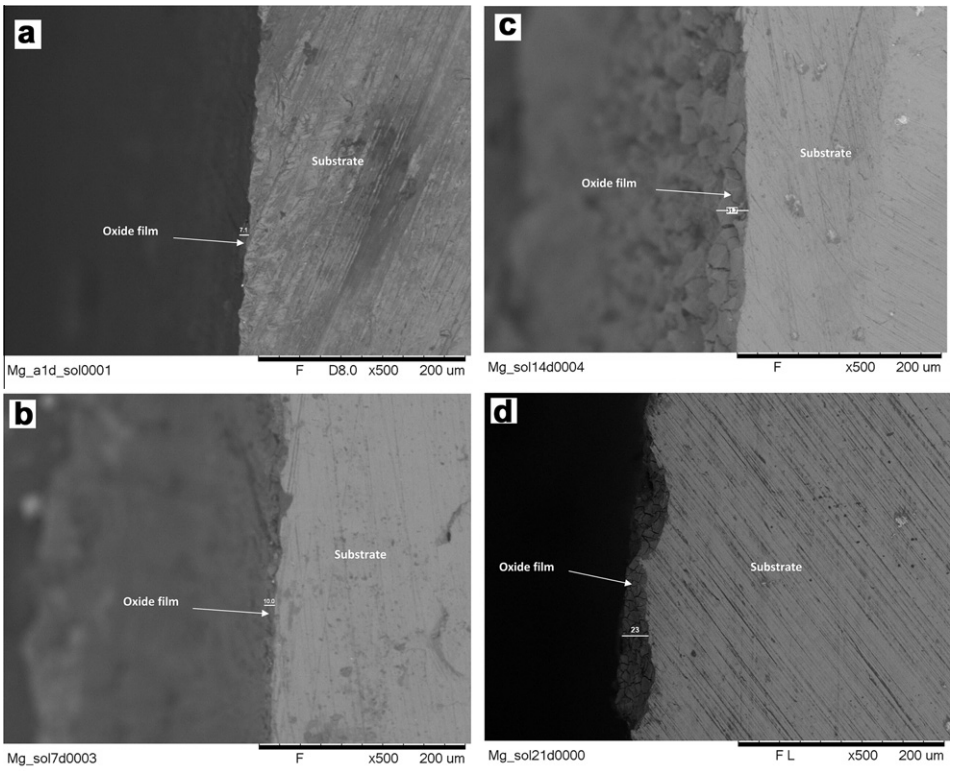


**Fig. 6.** SEM micrographs of the cross-sections of the SA specimens after different periods of immersion in 0.05 M $H_3BO_3$ + 0.075 M $Na_2B_4O_7{\cdot}10H_2O$ solution with pH = 9.2 at room temperature: (a) 1 day; (b) 7 days; (c) 14 days; and (d) 21 days. The thicknesses of the oxide films are indicated in the micrographs (the values are in micrometers).

The corrosion mechanism of magnesium alloys has been reviewed by several authors [18,33,34]. It is generally agreed that in neutral or basic aqueous solutions the following overall reaction takes place:

$$Mg + 2H_2O \rightarrow Mg(OH)_2 + H_2 \quad (3)$$

According to this reaction, a stable corrosion product forms and hydrogen gas bubbles evolve during anodic dissolution of the α-Mg. Indeed, this phenomenon was observed for the as-cast and SA specimens of the AZ91D alloy right after immersion and during the first 24 h. For longer immersion times the gas evolution ceased and an apparently thicker and denser oxide layer developed on the surface of the specimens. SEM micrographs of cross-sections of both the as-cast and SA specimens after different periods of immersion are displayed in Figs. 5 and 6, respectively. It is observed that the thickness of the oxide layer increases continuously from 1 to 21 days of immersion for both the as-cast and SA specimens.

The electrochemical behavior is markedly different for longer immersion times. Initially, it is easily recognized that the LF inductive loop disappeared from 7 days of immersion up to the end of the experiments. It is noteworthy that this fact apparently confirms the report by Anik and Celikten [31] who observed the suppression of the LF inductive loop as a protective oxide layer formed on the surface of an AZ91 alloy. Furthermore, as shown in Fig. 4b the impedance values presented a sharp increase after 7 days of immersion. This effect is also a manifestation of the formation of a more protective oxide film on the surface of the electrodes with time. The phenomenon occurs for both the SA and as-cast specimens, but it is more prominent for the last one, as attested by the higher radius of the semi-circle that characterizes the capacitive loop in lower frequencies. The same tendency is promptly identified for 14 and 21 days of immersion. The radius of the capacitive loop continues to increase with time for the as-cast and SA specimens, suggesting that the protective character of the oxide layer has an ascending nature. This is probably related to the thickness of the oxide films shown in the cross-sectional views of Figs. 5 and 6. It is also evident that the impedance values of the SA-specimen are surpassed by those of the as-cast one.

### 3.3.2. Potentiodynamic polarization curves

Potentiodynamic polarization curves of as-cast and SA specimens for different immersion times in 0.05 M $H_3BO_3$ + 0.075 M $Na_2B_4O_7{\cdot}10H_2O$ solution with pH = 9.2 at room temperature are shown in Fig. 7. Table 1 shows the electrochemical data obtained from polarization curves. The data correspond to the mean values of three different specimens tested at each condition. The values of corrosion current density ($I_{corr}$) were determined using the Tafel's extrapolation method.

The evolution of the electrochemical behavior of both the as-cast and SA specimens confirms the EIS results, showing a trend of increasing corrosion resistance with time. The corrosion potential ($E_{corr}$) shifted to nobler values with time for the as-cast and SA specimens. Moreover, the polarization curves shifted to lower current densities with time. The variation of both $I_{corr}$ and $E_{corr}$ with time reveals that the corrosion resistance of the as-cast and SA specimens was enhanced. This is likely to due to the formation of a protective oxide layer on the surface of the specimens in contact with the electrolyte [35]. This assumption is supported by the SEM micrographs in Figs. 5 and 6 which clearly show the thickening of the oxide layer on both the as-cast and SA conditions with time.

The parameters in Table 1 evidence that the corrosion behavior of the untreated AZ91D alloy was modified by solution annealing. The untreated material presented higher $E_{corr}$ and lower $I_{corr}$ than the solution annealed alloy after 7, 14 and 21 days of immersion. This result corroborates those obtained from the EIS measurements. The reduction of the corrosion resistance of the AZ91D after solution annealing is closely related to the undermining of the β-phase. Notwithstanding, there was an opposite behavior after 1 day of immersion. In order to give a further understanding into the corrosion mechanism active during the initial period of immersion we performed an immersion test according to the same conditions employed for the electrochemical measurements. Specimens of the as-cast and SA AZ91D alloy were immersed in 0.05 M $H_3BO_3$ + 0.075 M $Na_2B_4O_7{\cdot}10H_2O$ solution with pH = 9.2 at room temperature for 1 day. Optical micrographs were taken from the surface of the specimens at specific intermediate periods of immersion up to 1 day. The aim of this procedure was to study the role of the microstructure of the alloy on the initial corrosion attack. Thus, the micrographs were obtained after 10 min, 1 h, 4 h, 8 h and 24 h of immersion as shown in Figs. 8 and 9 for the as-cast and SA alloy, respectively. Micrographs of the specimens in the as-prepared condition (non-immersed) are also shown. The as-cast alloy showed a preferential dissolution of the eutectic α-phase along the grain boundaries in the vicinity of the β-phase. This effect was progressively intensified from 10 min (Fig. 8b) to 8 h of immersion (Fig. 8e), leading to a complete undermining of the β-phase. This effect was observed by Song et al. [15] for the AZ91D alloy. One possible explanation is that the grains of the α-phase are highly polarized due to the presence of the cathodic β-phase along the grain boundaries, leading to a strong galvanic effect and the prefer-

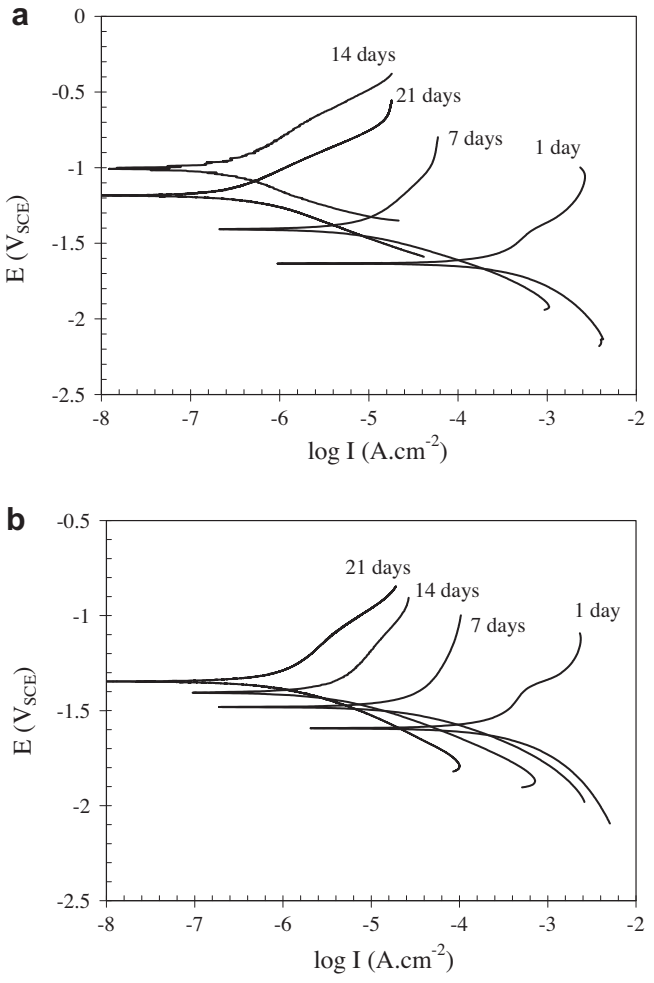


**Fig. 7.** Potentiodynamic polarization curves of the AZ91D specimens for different immersion times in 0.05 M $H_3BO_3$ + 0.075 M $Na_2B_4O_7{\cdot}10H_2O$ solution with pH = 9.2 at room temperature: (a) as-cast; and (b) SA.

**Table 1**
Electrochemical data obtained from potentiodynamic polarization curves. The data correspond to the mean values of three different specimens tested at each condition.

| Immersion (days) | $E_{corr}$ (V) | $I_{corr}$ (μA cm$^{-2}$) | $b_a$ (V/decade) | $\|b_c\|$ (V/decade) |
|---|---|---|---|---|
| *As-cast* | | | | |
| 1 | −1.61 ± 0.02 | 220 ± 21.0 | 0.443 ± 0.042 | 0230 ± 0.011 |
| 7 | −1.42 ± 0.03 | 6.90 ± 0.86 | 0.406 ± 0.058 | 0.165 ± 0.013 |
| 14 | −1.03 ± 0.06 | 0.21 ± 0.07 | 0.246 ± 0.036 | 0.169 ± 0.020 |
| 21 | −1.17 ± 0.05 | 0.28 ± 0.05 | 0.299 ± 0.038 | 0.159 ± 0.016 |
| *SA* | | | | |
| 1 | −1.55 ± 0.02 | 209 ± 10.6 | 0.425 ± 0.026 | 0.212 ± 0.015 |
| 7 | −1.50 ± 0.02 | 31.0 ± 7.55 | 0.380 ± 0.021 | 0.146 ± 0.010 |
| 14 | −1.42 ± 0.03 | 4.70 ± 1.82 | 0.572 ± 0.179 | 0.157 ± 0.024 |
| 21 | −1.52 ± 0.03 | 1.46 ± 0.57 | 0.519 ± 0.137 | 0.182 ± 0.026 |

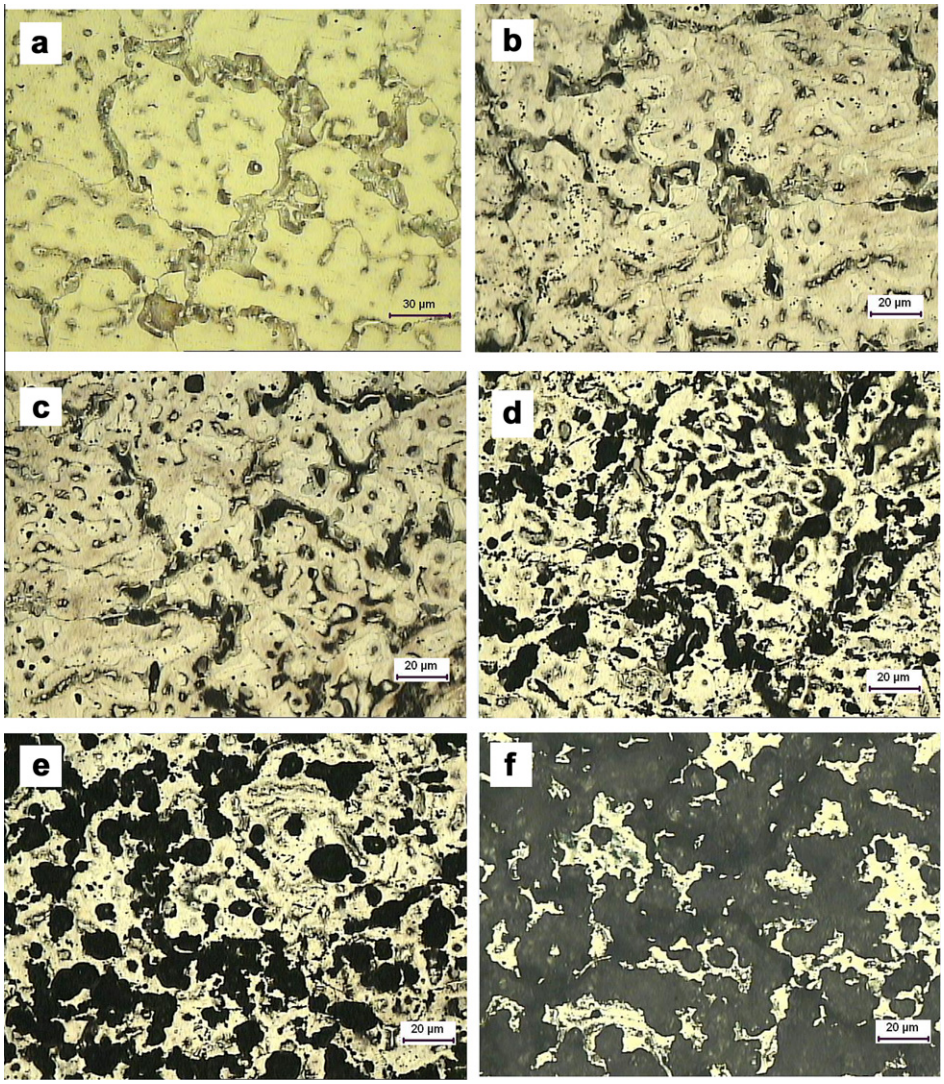


**Fig. 8.** Optical micrographs of the as-cast AZ91D alloy immersed for different times in 0.05 M $H_3BO_3$ + 0.075 M $Na_2B_4O_7{\cdot}10H_2O$ solution with pH = 9.2 at room temperature: (a) non-immersed; (b) 10 min; (c) 1 h; (d) 4 h; (e) 8 h; and (f) 24 h.

ential dissolution of the more anodic α-phase. Ultimately, with the undermining of the β-phase, the corrosion process spreads out throughout the primary α-phase within the grains of the matrix. The final morphology observed after 24 h of immersion (Fig. 8f) confirms this hypothesis. Once the oxide layer is developed, it starts acting as a barrier to the corrosion attack. Consequently, $I_{corr}$ decreases from 1 to 7 days of immersion as seen in Table 1.

The SA treatment dissolved the β-phase. As seen in the Fig. 9, this microstructural change altered the corrosion mechanism of the AZ91D alloy during the initial periods of immersion. The corrosion attack started within the α-Mg matrix, spreading throughout the whole surface as the immersion time increased from 10 min (Fig. 9b) to 8 h (Fig. 9e). However, the attack slower than occurred with the as-cast alloy. This is probably related to the large anodic area submitted to corrosion, giving rise to a smaller current density in comparison with the as-cast alloy, in which the anodic area was smaller due to the presence of the β-phase, giving rise to a higher corrosion current density. It is also interesting to note that some areas were not completely corroded on the surface of the SA alloy whereas the oxide coverage was more

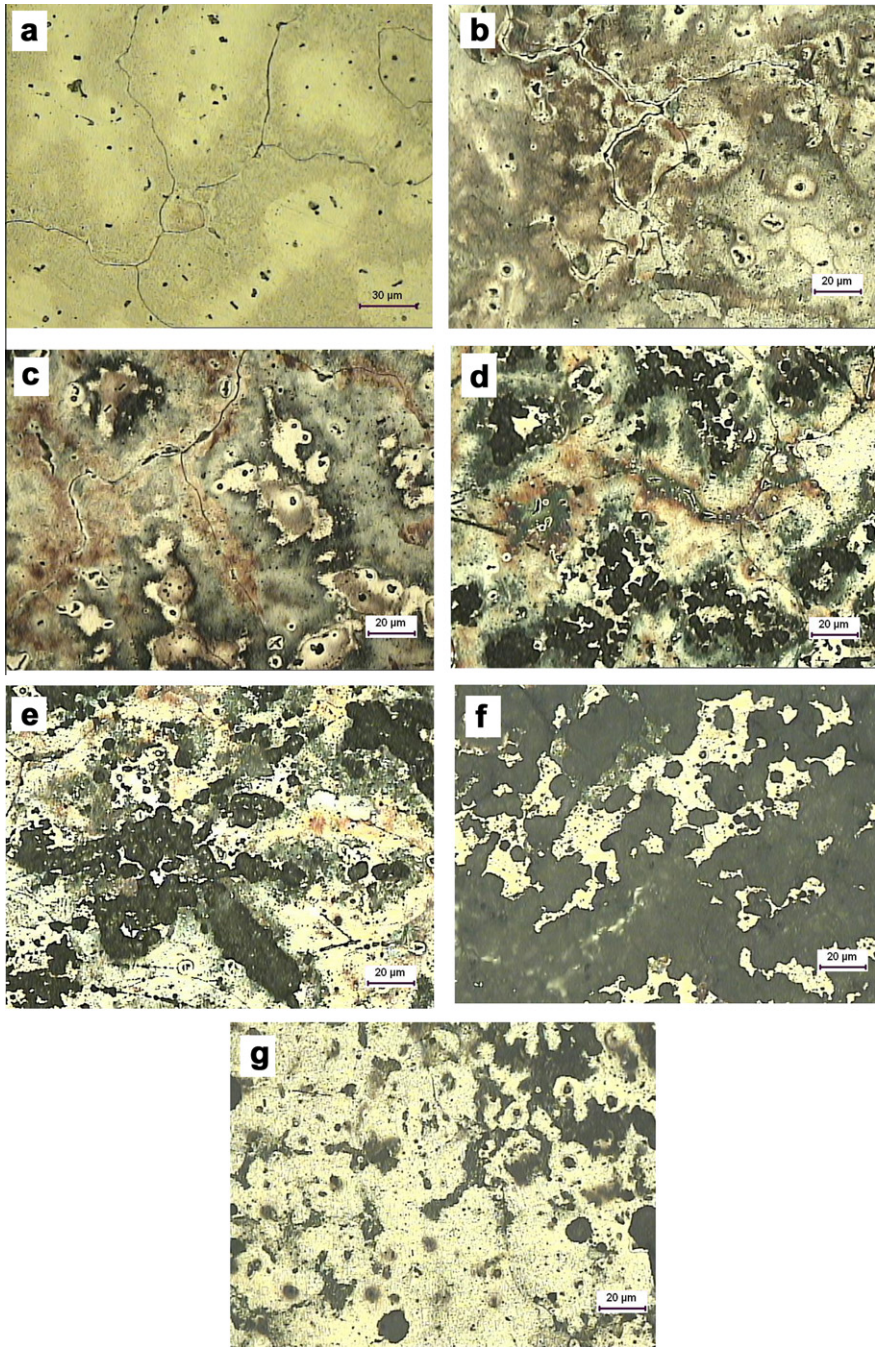


**Fig. 9.** Optical micrographs of the SA AZ91D alloy immersed for different times in 0.05 M $H_3BO_3$ + 0.075 M $Na_2B_4O_7{\cdot}10H_2O$ solution with pH = 9.2 at room temperature: (a) non-immersed; (b) 10 min; (c) 1 h; (d) 4 h; (e) 8 h; and (f) 24 h.

intense in the as-cast specimen. An example of an area with less corrosion products on the surface of the SA alloy is shown in Fig. 9g. It has to be emphasized, though, that most part of the surface was corroded as seen in Fig. 9f. In this context, the lower $I_{corr}$ of the SA alloy in comparison with the as-cast one after 1 day of immersion (see Table 1) can be explained by the mechanism observed in Fig. 9. For longer immersion times the entire surfaces were completely covered by a progressively thicker oxide layer as shown in Figs. 5 and 6 for both the as-cast and SA specimens. The thickness of the oxide film was higher for the as-cast specimen. The mechanism proposed here can justify the thickening of the oxide film with time for the as-cast specimen, while this would be more difficult for the SA alloy. Thus, the barrier effect of the thick oxide film would dominate the corrosion process, giving rise to higher impedance and lower $I_{corr}$ values for both the as-cast and SA alloy after 7 days and for longer immersion times.

### 3.4. Semiconducting properties of the oxide film

Mott–Schottky plots of the as-cast and solution annealed specimens acquired after 1, 7, 14 and 21 days of immersion in 0.05 M $H_3BO_3$ + 0.075 M $Na_2B_4O_7{\cdot}10H_2O$ solution with pH = 9.2 at room temperature are shown in Fig. 10.

From the Mott–Schottky plots it stands out that the electronic properties of the oxide films on the as-cast and SA specimens changes with time. It is seen that the curves obtained for 1 day

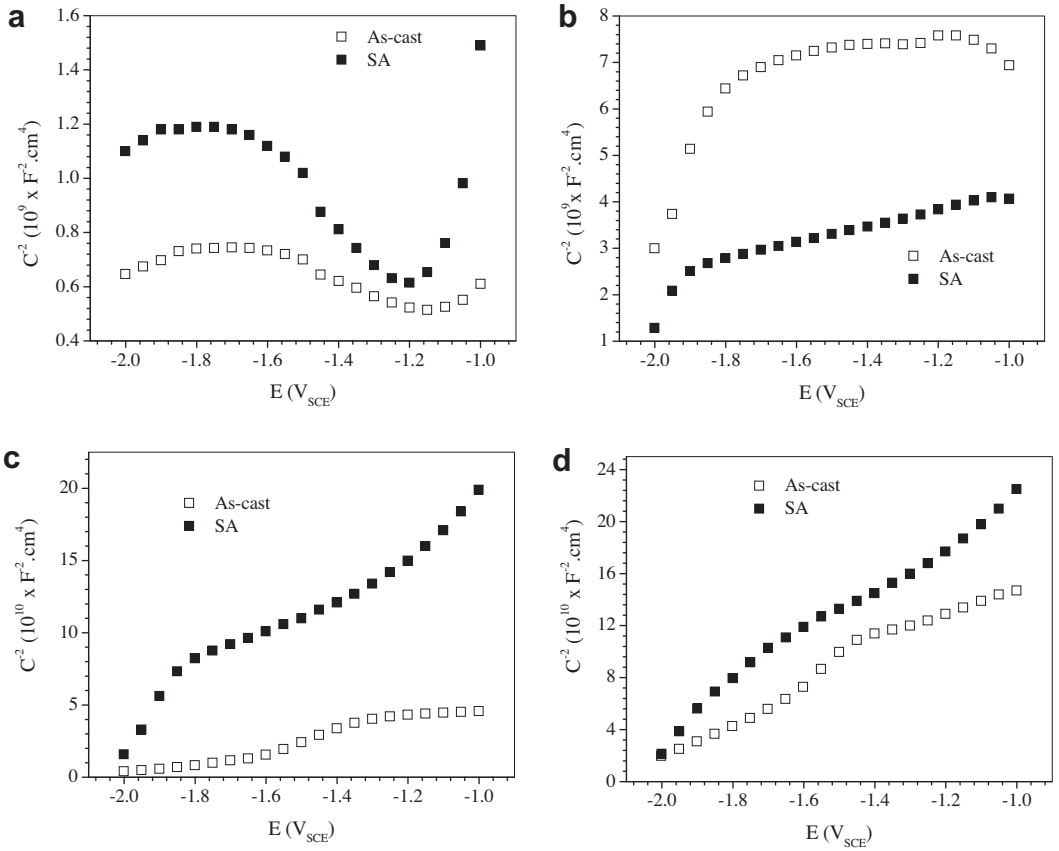


**Fig. 10.** Mott–Schottky plots of the as-cast and solution annealed specimens in 0.05 M $H_3BO_3$ + 0.075 M $Na_2B_4O_7{\cdot}10H_2O$ solution with pH = 9.2 at room temperature after different periods of immersion: (a) 1 day; (b) 7 days; (c) 14 days; and (d) 21 days.

**Table 2**
Charge carrier concentration in the oxide film formed on the as-cast and solution annealed specimens in 0.05 M $H_3BO_3$ + 0.075 M $Na_2B_4O_7{\cdot}10H_2O$ solution with pH = 9.2 at room temperature after different periods of immersion. The data correspond to the mean values of three different specimens tested at each condition.

| Condition | $N_q$ ($cm^{-3}$) Immersion (days) | | | |
|---|---|---|---|---|
| | 1 | 7 | 14 | 21 |
| As-cast | $2.91 \times 10^{22} \pm 3.84 \times 10^{20}$ | $1.83 \times 10^{22} \pm 2.63 \times 10^{20}$ | $2.90 \times 10^{20} \pm 9.40 \times 10^{17}$ | $1.06 \times 10^{20} \pm 3.07 \times 10^{18}$ |
| SA | $1.21 \times 10^{22} \pm 1.40 \times 10^{20}$ | $8.50 \times 10^{21} \pm 1.24 \times 10^{20}$ | $9.95 \times 10^{19} \pm 3.20 \times 10^{17}$ | $8.14 \times 10^{19} \pm 1.31 \times 10^{18}$ |

of immersion present a negative slope from $-1.2$ $V_{SCE}$ downward to more cathodic potentials. This variation of the capacitance with the applied potential is typical of a p-type semiconductor [36]. Zhang et al. [37] showed that hydrogen adsorbed on the surface of magnesium can give rise to a p-type semiconducting behavior, generating magnesium vacancies in the oxide layer which would be the major charge carriers in the film. The same authors [38] reported that a similar behavior was observed for the AZ91D alloy. As already mentioned in Section 3.2.1 hydrogen gas bubbles evolved during dissolution of both the as-cast and SA specimens up to first day of immersion. The p-type behavior observed in the corresponding Mott–Schottky plots (Fig. 10a) would be a consequence of the hydrogen bubbles formed during the initial corrosion process of the alloy. As a thicker and more compact oxide film developed with time, the evolution of gas bubbles ceased. Consequently, the adsorption of hydrogen gas on the surface of the electrodes was no longer possible. Then, the slope of the Mott–Schottky plots became positive from 7 up to 21 days of immersion, indicating that the semiconducting character of the oxide film was altered to that of an n-type semiconductor [39]. Both the as-cast and SA specimens assumed the n-type semiconductivity. For this type of behavior, the main defects in the oxide film are cation interstitials or anion vacancies [40]. Duan et al. [41] observed that the oxide layer on the AZ91D alloy presented an n-type behavior when immersed in a 0.1 M $Na_2B_4O_7{\cdot}10H_2O$ + 0.05 M NaCl solution. Heakal et al. [19] have also found an n-type behavior for the oxide film formed on the AZ91D alloy upon immersion in a borate solution.

Depending if the oxide film behaves as a p-type or n-type semiconductor, the corresponding acceptors (magnesium vacancies) or donors (mainly oxygen vacancies) can be calculated from the slope of the linear portion of the Mott–Schottky plots. This concentration corresponds to the number of defects in the film. A high doping density is typical of a defective oxide layer which, in turn, is associated with a lower corrosion resistance [42]. The charge carrier concentrations corresponding to the mean values of three different specimens tested at each condition are shown in Table 2.

The highest charge carrier concentrations were found after 1 day of immersion. According to Carmezim et al. [43] this is a clear

indication of a highly disordered oxide film. As already mentioned, the oxide layer behaved as a p-type semiconductor after 1 day of immersion. In this case, the defects are mainly cation vacancies. As seen in Table 2, the number of defects continuously diminished with time for the as-cast and SA specimens. For longer periods of immersion the oxide film presented an n-type character. Oxygen vacancies and cation interstitials are the main defects in this case, acting as electron donors. It has been reported that the presence of such doping species in the oxide film hampers the migration of cations from the metallic materials underneath the oxide layer. The same occurs with the penetration of aggressive anions from the electrolyte, such as $Cl^-$ and $SO_4^-$ [44]. In this regard the corrosion resistance would increase when the semiconducting character of the oxide film changes from p-type to n-type. The reduction of the number of defects in the oxide film with time revealed in Table 2 also points to the formation of less conductive and more protective oxide layers. This result confirms the increase of corrosion resistance with time observed from the Nyquist plots and potentiodynamic polarization curves for both the as-cast and SA specimens.

## 4. Conclusions

The solution annealing treatment was effective at dissolving the β-$Mg_{17}Al_{12}$ phase. The corrosion resistance of the AZ91D alloy increased with the time of immersion in the 0.05 M $H_3BO_3$ + 0.075 M $Na_2B_4O_7{\cdot}10H_2O$ solution with pH = 9.2 at room temperature for both the as-cast and solution annealed conditions. This behavior could be explained based on the thickness increase of the oxide film formed on the surface of the alloy with time as revealed by the SEM micrographs. The results from EIS measurements and potentiodynamic polarization curves indicated that the solution treatment decreased the corrosion resistance of the AZ91D alloy. The increase of the corrosion resistance with the immersion time was accompanied by the decrease of the charge carrier concentration in the oxide films formed on the as-cast and solution annealed specimens. The Mott–Schottky plots showed that the semiconducting behavior of the oxide films changed from p-type after 1 day of immersion to n-type for longer periods for both the as-cast and solution annealed specimens.

## Acknowledgment

The authors are thankful to Rima Industrial Magnésio S/A for kindly providing the ingot of the AZ91D alloy used in this work.

## References

[1] P.D. Beggs, W. Song, M. Easton, Failure modes during uniaxial deformation of magnesium alloy AZ31B tubes, Int. J. Mech. Sci. 52 (2010) 1634–1645.
[2] X. Chen, G. Li, J. Lian, Q. Jiang, An organic chromium-free conversion coating on AZ91D magnesium alloy, Appl. Surf. Sci. 255 (2008) 2322–2328.
[3] Z. Trojanová, P. Lukác, H. Ferkel, W. Riehemann, Internal friction in microcrystalline and nanocrystalline Mg, Mater. Sci. Eng., A 370 (2004) 154–157.
[4] E. Aghion, N. Moscovitch, A. Arnon, The correlation between wall thickness and properties of HPDC Magnesium alloys, Mater. Sci. Eng., A 447 (2007) 341–346.
[5] Y. Xin, T. Hu, P.K. Chu, In vitro studies of biomedical magnesium alloys in a simulated physiological environment: a review, Acta Biomater. 7 (2011) 1452–1459.
[6] S.E. Harandi, M.H. Idris, H. Jafari, Effect of forging process on microstructure, mechanical and corrosion properties of biodegradable Mg–1Ca alloy, Mater. Des. 32 (2011) 2596–2603.
[7] A.F. Galio, S.V. Lamaka, M.L. Zheludkevich, L.F.P. Dick, I.L. Müller, M.G.S. Ferreira, Inhibitor-doped sol–gel coatings for corrosion protection of magnesium alloy AZ31, Surf. Coat. Technol. 204 (2010) 1479–1486.
[8] Y. Tao, T. Xiong, C. Sun, L. Kong, X. Cui, T. Li, G.L. Song, Microstructure and corrosion performance of a cold sprayed aluminium coating on AZ91D magnesium alloy, Corros. Sci. 52 (2010) 3191–3197.
[9] N.I.Z. Abidin, D. Martin, A. Atrens, Corrosion of high purity Mg, AZ91, ZE41 and Mg2Zn0.2Mn in Hank's solution at room temperature, Corros. Sci. 53 (2011) 862–872.
[10] Y.C. Lin, X.M. Chen, G. Chen, Uniaxial ratcheting and low-cycle fatigue failure behaviors of AZ91D magnesium alloy under cyclic tension deformation, J. Alloys Compd. 509 (2011) 6838–6843.
[11] G. Ballerini, U. Bardi, R. Bignucolo, G. Ceraolo, About some corrosion mechanisms of AZ91D magnesium alloy, Corros. Sci. 47 (2005) 2173–2184.
[12] S. Mathieu, C. Rapin, J. Hazan, P. Steinmetz, Corrosion behaviour of high pressure die-cast and semi-solid cast AZ91D alloys, Corros. Sci. 44 (2002) 2737–2756.
[13] A. Pardo, M.C. Merino, A.E. Coy, R. Arrabal, F. Viejo, E. Matykina, Corrosion behaviour of magnesium/aluminium alloys in 3.5 wt.% NaCl, Corros. Sci. 50 (2008) 823–834.
[14] W. Zhou, T. Shen, N.N. Aung, Effect of heat treatment on corrosion behaviour of magnesium alloy AZ91D in simulated body fluid, Corros. Sci. 52 (2010) 1035–1041.
[15] G. Song, A. Atrens, M. Dargusch, Influence of microstructure on the corrosion of diecast AZ91D, Corros. Sci. 41 (1999) 249–273.
[16] N.N. Aung, W. Zhou, Effect of heat treatment on corrosion and electrochemical behaviour of AZ91D magnesium alloy, J. Appl. Electrochem. 32 (2002) 1397–1401.
[17] R. Ambat, N.N. Aung, W. Zhou, Evaluation of microstructural effects on corrosion behaviour of AZ91D magnesium alloy, Corros. Sci. 42 (2000) 1433–1455.
[18] K.W. Guo, A review of magnesium/magnesium alloys corrosion and its protection, Recent Patent Corros. Sci. 2 (2010) 13–21.
[19] F.E.T. Heakal, A.M. Fekry, M.A.E.B. Jibril, Electrochemical behavior of the Mg alloy AZ91D in borate solutions, Corros. Sci. 53 (2011) 1174–1185.
[20] Y. Li, T. Zhang, F. Wang, Effect of microcrystallization on corrosion resistance of AZ91D alloy, Electrochim. Acta 51 (2006) 2845–2850.
[21] S. Modiano, C.S. Fugivara, A.V. Benedetti, Effect of citrate ions on the electrochemical behaviour of low-carbon steel in borate buffer solutions, Corros. Sci. 46 (2004) 529–545.
[22] E.M.A. Martini, I.L. Muller, Characterization of the film formed on iron in borate buffer solution by electrochemical impedance spectroscopy, Corros. Sci. 42 (2000) 443–454.
[23] S.J. Xia, R. Yue, R.G. Rateick Jr., V.I. Briss, Electrochemical studies of AC/DC anodized Mg alloy in NaCl solution, J. Electrochem. Soc. 151 (2004) B179–B187.
[24] G. Song, A. Atrens, D. St John, X. Wu, J. Nairn, The anodic dissolution of magnesium in chloride and sulphate solutions, Corros. Sci. 39 (1997) 1981–2004.
[25] G. Song, A. Atrens, X. Wu, B. Zhang, Corrosion behaviour of AZ21, AZ501 and AZ91 in sodium chloride, Corros. Sci. 40 (1998) 1769–1791.
[26] G. Galicia, N. Pébère, B. Tribollet, V. Vivier, Local and global electrochemical impedances applied to the corrosion behaviour of an AZ91 magnesium alloy, Corros. Sci. 51 (2009) 1789–1794.
[27] G. Baril, G. Galicia, C. Deslouis, N. Pébère, B. Tribollet, V. Vivier, An impedance investigation of the mechanism of pure magnesium corrosion in sodium sulfate solutions, J. Electrochem. Soc. 154 (2007) C108–C113.
[28] T. Zhang, Y. Shao, G. Meng, Z. Cui, F. Wang, Corrosion of hot extrusion AZ91 magnesium alloy: I-relation between the microstructure and corrosion behavior, Corros. Sci. 53 (2011) 1960–1968.
[29] J. Chen, J. Wang, E. Han, J. Dong, W. Ke, AC impedance spectroscopy study of the corrosion behavior of an AZ91 magnesium alloy in 0.1 M sodium sulfate solution, Electrochim. Acta 52 (2007) 3299–3309.
[30] G. Baril, N. Pébère, The corrosion of pure magnesium in aerated and deaerated sodium sulphate solutions, Corros. Sci. 43 (2001) 471–484.
[31] M. Anik, G. Celikten, Analysis of the electrochemical reaction behavior of alloy AZ91 by EIS technique in $H_3PO_4$/KOH buffered $K_2SO_4$ solutions, Corros. Sci. 49 (2007) 1878–1894.
[32] F. Zucchi, V. Grassi, A. Frignani, C. Monticelli, G. Trabanelli, Electrochemical behavior of a magnesium alloy containing rare earth elements, J. Appl. Electrochem. 36 (2006) 195–204.
[33] E. Ghali, W. Dietzel, K.U. Kainer, General and localized corrosion of magnesium alloys: a critical review, J. Mater. Eng. Perform. 13 (2004) 7–23.
[34] A. Atrens, M. Liu, N.I.Z. Abidin, Corrosion mechanism applicable to biodegradable magnesium implants, Mater. Sci. Eng., B 176 (2011) 1609–1636.
[35] R. Arrabal, A. Pardo, M.C. Merino, M. Mohedano, P. Casajús, K. Paucar, G. Garcés, Effect of Nd on the corrosion behaviour of AM50 and AZ91D magnesium alloys in 3.5 wt.% NaCl solution, Corros. Sci. 55 (2012) 301–312.
[36] L. Hamadou, A. Kadri, N. Benbrahim, Impedance investigation of thermally formed oxide films on AISI 304L stainless steel, Corros. Sci. 52 (2010) 859–864.
[37] T. Zhang, Y. Shao, G. Meng, Y. Li, F. Wang, Effects of hydrogen on the corrosion of pure magnesium, Electrochim. Acta 52 (2006) 1323–1328.
[38] T. Zhang, Y. Li, F. Wang, Roles of β phase in the corrosion process of AZ91D magnesium alloy, Corros. Sci. 48 (2006) 1249–1264.
[39] R.A. Antunes, M.C.L. De Oliveira, I. Costa, Study of the correlation between corrosion resistance and semi-conducting properties of the passive film of AISI 316L stainless steel in physiological solution, Mater. Corros. 63 (2012) 586–592.
[40] J. Liu, D.D. Macdonald, The passivity of iron in the presence of ethylenediaminetetracetic acid. II The defect and electronic structures of the barrier layer, J. Electrochem. Soc. 148 (2001) B425–B430.

[41] H. Duan, C. Yan, F. Wang, Effect of electrolyte additives on performance of plasma electrolytic oxidation films formed on magnesium alloy AZ91D, Electrochim. Acta 52 (2007) 3785–3793.
[42] S. Ningshen, U.K. Mudali, V.K. Mittal, H.S. Khatak, Semiconducting and passive film properties of nitrogen-containing type 316LN stainless steels, Corros. Sci. 49 (2007) 481–496.
[43] M.J. Carmezim, A.M. Simões, M.O. Figueiredo, M. Da Cunha Belo, Electrochemical behaviour of thermally treated Cr-oxide films deposited on stainless steel, Corros. Sci. 44 (2002) 451–465.
[44] G. Goodlet, S. Faty, S. Cardoso, P.P. Freitas, A.M.P. Simões, M.G.S. Ferreira, M. Da Cunha Belo, The electronic properties of sputtered chromium and iron oxide films, Corros. Sci. 46 (2004) 1479–1499.